Pergamon

Int. J. Impact Engng Vol. 16, No. 1, pp. 119–132, 1995
Elsevier Science Ltd
Printed in Great Britain
0734–743X/95 $9.50 + 0.00

0734–743X(94)00031-X

DYNAMIC RESPONSES OF A KINETIC ENERGY PROJECTILE UNDER TRANSVERSE LOADINGS

R. H. ALLEN

Department of Mechanical Engineering, University of Delaware, Newark, DE 19716-3140, U.S.A.

(*Received* 20 *October* 1993; *in revised form* 20 *April* 1994)

Summary—We report on the effects of launch tube nonstraightness and asymmetric loading on the accuracy performance of a kinetic energy projectile. Modeling the projectile as a rigid body within the launch tube, we obtain and solve the equations of rotary motion to calculate the orientation of the projectile relative to the tube as a function of time. Three launch tube geometries are modeled; curiously, the most severe environment does not produce the most deviant projectile orientations during in-bore travel or at muzzle exit. To determine the effects of asymmetric loading, we model the rod as a nonuniform two-dimensional beam, subject to a transverse blast load. Determined experimentally, the sabot equivalent stiffness is bounded between 10^6 and 10^7 N/m. These bounds are used in an elastic boundary condition to the rod finite element model. The ANSYS transient vibration analyses predict a peak transverse displacement of 20 mm and a peak transverse velocity of 75 mm/s at muzzle exit. We conclude that: (1) base pressures asymmetry induces transverse vibrations in the projectile, and these vibrations are affected by sabot stiffness; and (2) launch tube profile nonstraightness induces rigid body rotations in the projectile, and these rotations may or may not increase with launch tube severity.

NOTATION

θ_p	projectile angle measured from the horizontal
θ_T	gun tube slope
θ	projectile angle measured from the gun tube slope
I_1	mass moment of inertia about rear obturator contact point
I_2	mass moment of inertia about forward bell contact point
M	projectile mass
R	half diagonal distance between rear obturator and forward bell
α	$\tan^{-1}$ obturator bell spacing/projectile height
c	rebound velocity coefficient
t_0	time of most recent impact
O_1	rear obturator contact point
O_2	forward bell contact point

1. INTRODUCTION

Kinetic energy projectiles (KEPs) distinguish themselves among other ammunition because they possess a unique range of mass—mean 4 kg—and achieve a unique range of velocities—average 1650 m/s. Used principally to defeat armor, KEPs need to be as accurate as possible. Several factors contribute to a KEP's performance. Among them: deviation from launch tube straightness [1,2], base pressure asymmetry [3,4], projectile design [5,6] and projectile flexibility [7].

These factors can contribute to inaccuracy by encouraging unintended orientations and angular velocities at launch exit, thereby affecting projectile trajectory. By understanding how these factors affect performance, we can suggest methods and alternative designs to minimize adverse affects.

One promising projectile, depicted schematically in Fig. 1, is the DM13. Like other projectiles, this one has four major components: a penetrating rod, a three-piece sabot system, a five-petalled fin that screws onto the base of the rod, and a tapered windscreen and tip that are press-fit onto the front of the rod. Figure 2 shows a photograph of a

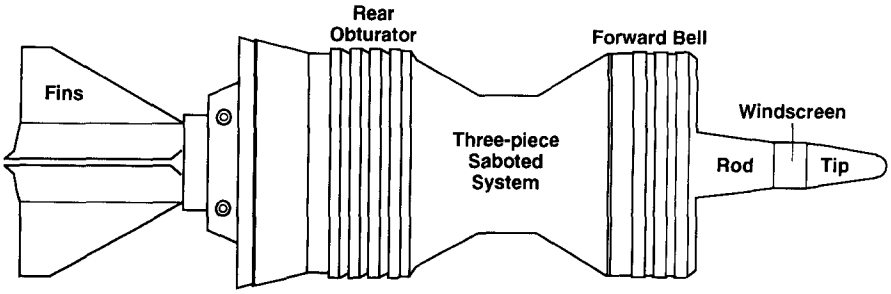

Fig. 1. Schematic of DM13. Length of projectile is 470 mm; maximum height is 119.74 mm.

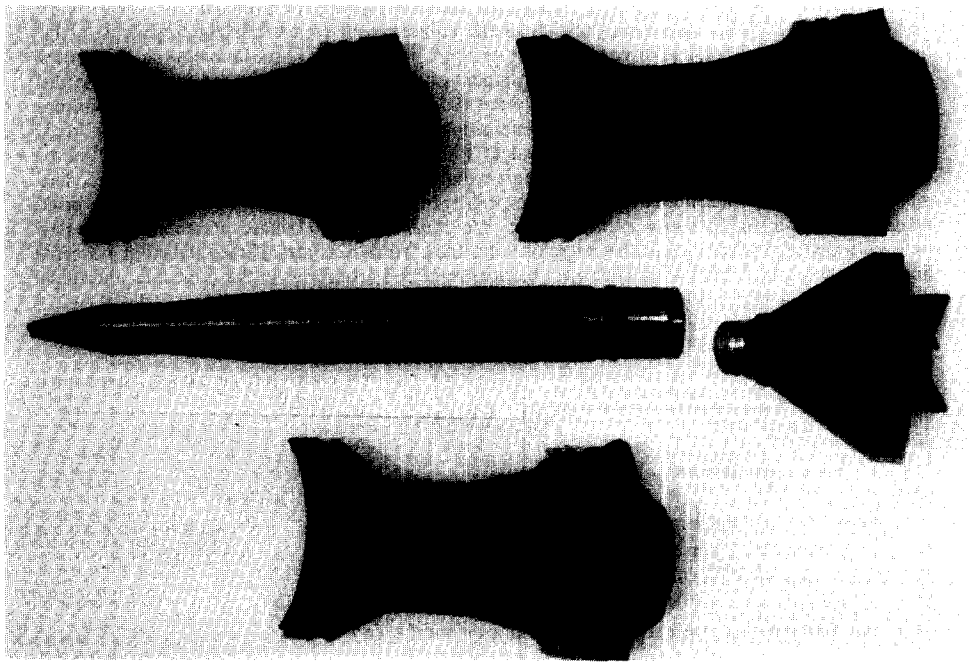

Fig. 2. Photograph of DM13 disassembled.

disassembled DM13 projectile. The windscreen and tip act in concert to reduce aerodynamic drag, and the fins stabilize the rod's motion during flight. As shown in Fig. 3, the three sabot petals separate from the penetrating rod microseconds after muzzle exit. The sabot is critical during in-bore travel because it provides lateral and axial support to the rod. The DM13 is low-cost and has good accuracy characteristics. Because of its foreign development and manufacture, however, little is known about the projectile's dynamic characteristics.

To begin quantifying the projectile's launch tube performance, we address two questions in this study

- What are the effects of launch tube nonstraightness on a rigid body idealization of the DM13?
- What are the effects of base pressure asymmetry on the transverse, transient vibrations of a two-dimensional finite element model of the projectile?

These questions are addressed in the following sections of this report.

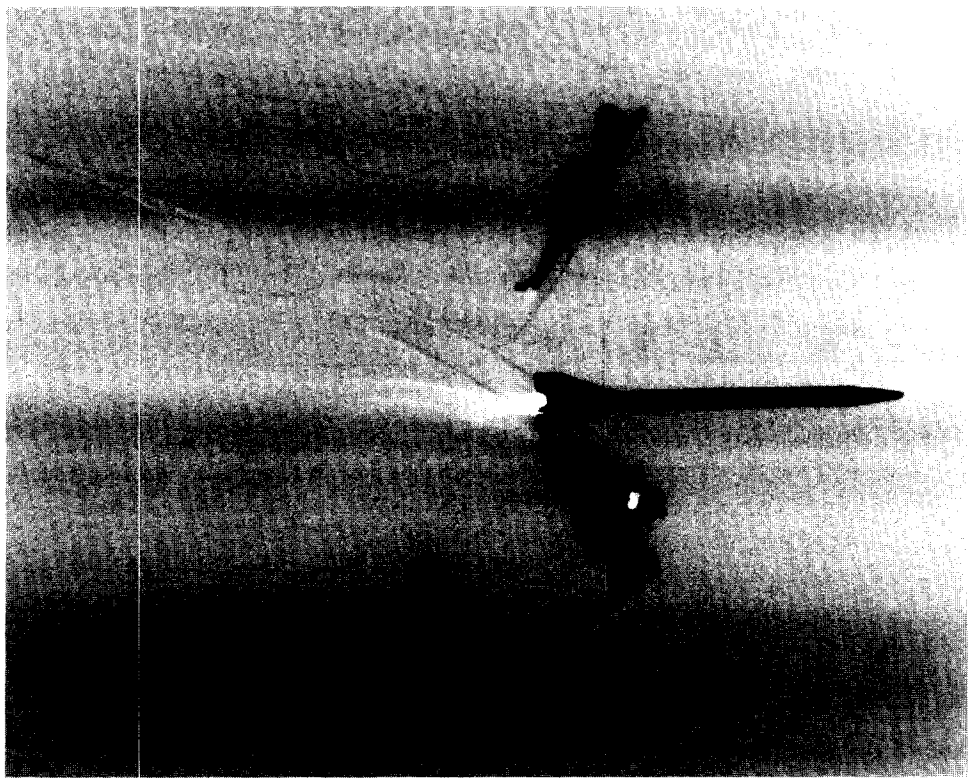

Fig. 3. Photograph of rod, windscreen and tip, and fins separating from a three-piece sabot system just after launch. Velocity at separation is about 1500 m/s.

2. RIGID BODY MODEL

One factor that can influence the accuracy performance of a KEP is rigid body rotation of the projectile within the launch tube. Although not addressed in previous launch tube reports, rigid body effects are known to play a role in inverted pendulums [8], shielding blocks [9], structural systems [10], and mechanical systems [11].

When a KEP rests on a horizontal surface, it is in contact with the surface at two points: the rear obturator and the forward bell (see Fig. 1). If the tip is elevated or lowered, the KEP rotates about the rear obturator contact point; when the fins are elevated or lowered, the KEP rotates about the forward bell contact point. When a KEP traverses a nonstraight launch tube, gaps occur between the tube wall and the projectile at the contact points due to the deflection and slope of the tube. These gaps induce the projectile to undergo rigid body rotation.

To isolate these rigid body rotations, we propose a two-dimensional rigid body model as depicted in Fig. 4. The projectile is shown at some arbitrary stand off distance from the reference plane and at an arbitrary angle of orientation with respect to the reference plane and with respect to the gun tube axis (local). Measured from the horizontal, the projectile angle is represented by θ_p while the launch tube angle is represened by θ_T. By summing moments about the rear obturator contact point, O_1, or the forward bell contact point, O_2, the equations of motion for small θ_p are:

$$I_1\ddot{\theta}-mgR\theta_p\cos\alpha=-mgR\sin\alpha \qquad \theta_p>\theta_T \tag{1}$$

$$I_2\ddot{\theta}_p-mgR\theta_p\cos\alpha=mgR\sin\alpha \qquad \theta_p<\theta_T$$

Here I_1 is the mass moment of inertia about O_1; I_2 is the mass moment of inertia about O_2; R is the half diagonal distance to to bottom between rear obturator and forward bell;

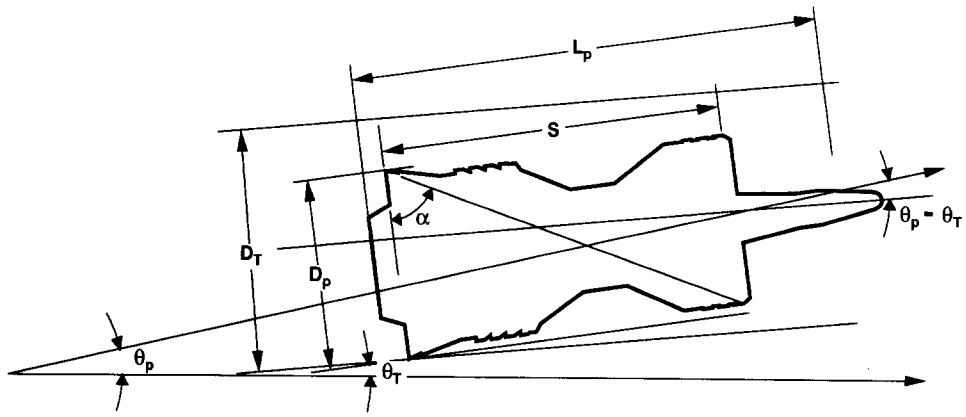

Fig. 4. Idealized model of projectile undergoing a rigid body rotation in launch tube. θ_p measures the projectile's angle, whereas θ_T measures the launch tube slope. Both angles are measured from the horizontal.

Table 1. Geometric and weight properties of the DM13 projectile

Property	*Value*
Diagonal, R	0.0994 m
Slenderness angle, α	0.9276 rad
Moment of inertia about O_1, I_1	5.47×10^5 g/cm^2
Moment of inertia about O_2, I_2	8.28×10^5 g/cm^2
Weight, mg	68.3 N

mg is the projectile weight, and α is the slenderness angle defined by the ratio of the wheel base (obturator bell spacing) and projectile height. Typical values for the DM13 are presented in Table 1.

We obtained R, α and mg by direct measurement; the moments of inertia, by calculations. Equation (1) can be written compactly as

$$\ddot{\theta}_p - p_1^2\theta_p = -p_1^2 \tan\alpha \qquad \theta_p > \theta_T \tag{2}$$

$$\ddot{\theta}_p - p_2^2\theta_p = p_2^2 \tan\alpha \qquad \theta_p < \theta_T$$

where $p_1^2 \equiv \dfrac{mgR}{I_1}\cos\alpha$ and $p_2^2 \equiv \dfrac{mgR\cos\alpha}{I_2}$

In comparison with the usual forms of the SDOF vibration equation, these forms of the governing differential equations are atypical for three reasons. First, the "stiffnesses' are negative. This leads to exponential solutions inherently more sensitive to parameters than conventional vibratory systems. Second, the "free vibration" equation contains an inhomogeneous term, which is nonlinear. Most importantly, each solution is valid for only one permutation in sign of θ_p. As a result, the overall response is not continuous; rather it is a series of local responses connected at points in time when $\theta_p = \theta_T$, the impact condition.

To solve the problem, then, we develop solutions for each sign permutation in θ_p. These are:

$$\theta_p(t) = \tan\alpha\,\mathrm{sgn}\theta + (\theta_o - \tan\alpha\,\mathrm{sgn}\theta)\cosh p_i(t-t_o) + (\dot{\theta}_{oi}p_i)\sinh p_i(t-t_o), \tag{3}$$

$$\dot{\theta}_p(t) = (\theta_o - \tan\alpha\,\mathrm{sgn}\theta)p_i\sinh p_i(t-t_o) + \dot{\theta}_o\cosh p_i(t-t_o).$$

Here,

$$\theta_o \equiv \theta_p(t_o),\ \dot{\theta}_o \equiv \dot{\theta}(t_o) \quad \text{and} \quad t_o \text{ being time of most recent impact}$$

$$\theta \equiv \theta_p - \theta_T, \quad \text{sgn}\theta = \begin{cases} 1 \text{ for } \theta > 0 \\ -1 \text{ for } \theta < 0 \end{cases}$$

$$i = 1 \text{ for } \theta > 0,$$

$$i = 2 \text{ for } \theta < 0.$$

One of these equations is valid for a given segment of rotation, but neither is valid for $\theta_p = \theta_T$, bottom impact, nor are they valid when $|\theta_p - \theta_T|$ is sufficiently large to cause impact with the top of the gun tube. At these impact conditions, conservation of moment of momentum dictates an instantaneous reduction in angular velocity. Expressed mathematically,

$$\theta_p(t+) = \theta_p(t-) \tag{4}$$
$$\dot{\theta}_p(t+) = c\dot{\theta}_p(t-)$$

where $t+$ is the time immediately after impact, $t-$ immediately before, and c is a rebound velocity coefficient, $0 < c < 1$. After impact occurs, a new segment of rotation begins and motion continues in this way until muzzle exit.

Two limiting assumptions used in developing this model are that it is two-dimensional and the projectile is unloaded. Because the projectile is axisymmetric, tube deflections the z direction are negigible, and gravity only acts vertically, a two-dimensional model should capture the rigid body rotation. Although base pressure asymmetry causes a tipping moment, we neglected it here because our goal is to isolate the effects of launch tube nonstraightness on the rocking response; we explore asymmetry effects in the vibration analysis.

To achieve the goal of studying geometry effects, we model three existing launch tube profiles: SN81, SN104 and SN5064. Thse profiles are depicted graphically in Fig. 5 as a function of tube axial location. Rabern obtained two tube gravity droop profiles—SN81 and SN104—by modeling the 5 m tubes as linear elastic cantilevers with ABAQUS [7].

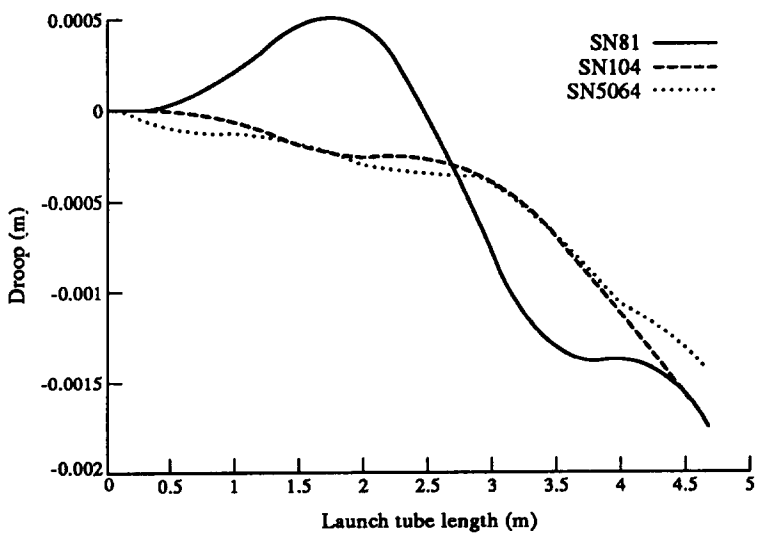

Fig. 5. Plot of vertical displacements of three launch tubes—SN81, SN104, and SN5064—as a function of tube location.

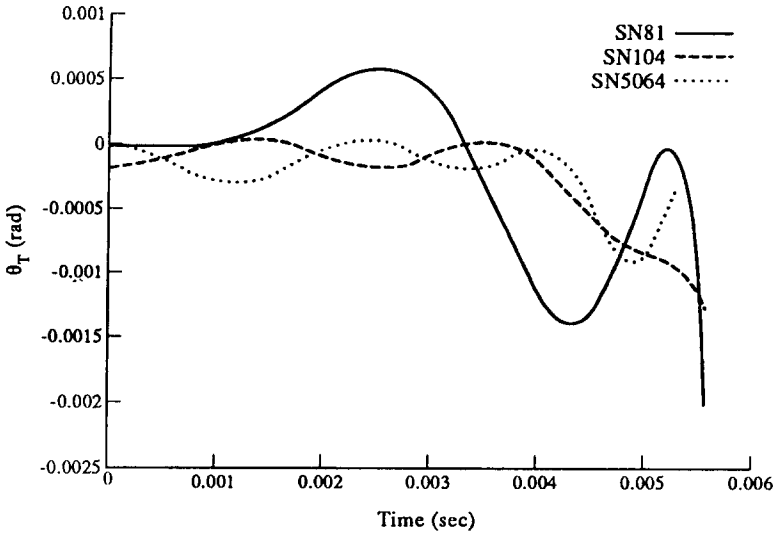

Fig. 6. Launch tube slopes for SN81, SN104, and SN5064 as a function of time. Slopes are measured from horizontal.

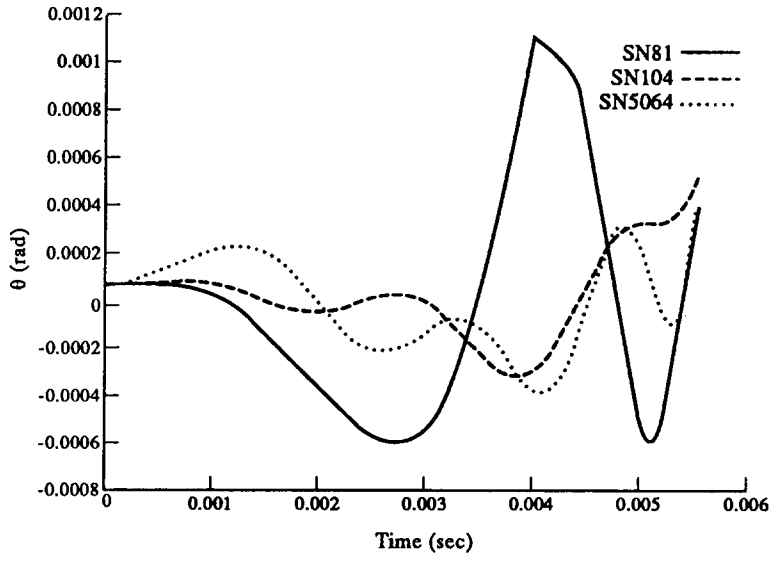

Fig. 7. Relative projectile rotations as a function of axial tube location for three launch tubes—SN81, SN104, and SN5064. Initial rotation in each case is 1×10^{-4} rad.

Wilkerson calculated the tube profile for tube SN5064 from optical field measurements [12]. Gravity droop causes a majority of the deformation in Fig. 5; deviations from linear elastic theory are due to imperfections in the straightness of the tube. Launch tube SN81 represents a severe environment, SN5064 represents a moderately bent tube, and SN104 represents a nearly straight tube.

Derived by numerically differentiating the total droop profile with respect to axial tube location, we obtain the slopes of the tubes. These slopes are plotted in Fig. 6 as a function of time. The transformation from space to time is made possible by Rabern's plot of axial location versus time [2]. Having θ_T as a function of time facilitates the solution methodology described earlier.

One set of solution results is presented in Figs 7 and 8. In Fig. 7, the projectile orientations, $\theta_p - \theta_T$ are plotted against time. The orientations are relative to their respective launch

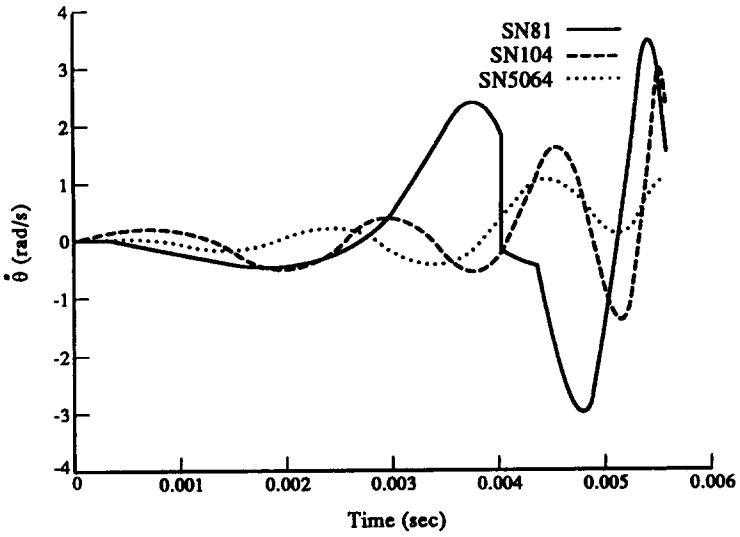

Fig. 8. Relative angular velocities of projectiles, $\dot{\theta}_p - \dot{\theta}_T$ as a function of axial tube location for three launch tubes—SN81, SN104, SN5064. Coefficient of rebound at impact is 0.8. Initial rotation in each case is 1×10^{-4} rad.

tube's slope assuming an initial rotation of 1×10^{-4} rad (0.0057°). A curve crossing the time axis corresponds to the forward bell impacting the lower tube wall. Only in tube SN81 (the most severe) does the projectile impact the upper tube wall (at 3.8 ms). At muzzle exit, the projectile orientations differ from the launch tube slopes; however, differences are limited to less than 8×10^{-4} rad (0.023°).

That the largest angular difference occurs with tube SN104 is surprising in that it is the straightest tube in the group. Other time histories, not shown, reveal similar results in the projectile orientations.

Figure 8 shows a plot of the relative angular velocity ($\dot{\theta}_p - \dot{\theta}_T$) histories of the projectile in each of the launch tubes. When the projectile impacts the upper surface of tube SN81, the angular velocity undergoes an instantaneous change in direction; this can be seen at $t = 3.8$ ms. Angular velocities achieve rates of 3 rad/s; but at muzzle exit peak velocity is about 2 rad/s. This peak occurs in launch tube SN5064. In all three tubes, the magnitudes of the projectile angular velocities are significant and similar to those predicted by Rabern [3,4], who explored loading asymmetry with three-dimensional finite element modeling techniques.

3. TRANSIENT VIBRATION ANALYSIS

To isolate the effects of base pressure asymmetry on the transverse response of the DM13 projectile, we develop a model that captures the loading on, geometric and material properties of, and support conditions to the projectile. The complex geometry and material nonunformity of the projectile rule out, or make intractable, a completely analytical solution; selecting and developing an appropriate finite element model thus becomes our goal.

The type of finite element model to be developed depends on several factors. Chief among them: (1) the class of problem to be modeled, (2) the results desired, and (3) the hardware, software and human resources available for the task. From Rabern's three-dimensional simulations, we know in general that projectiles acquire peak stresses below yield and undergo small transverse displacements and rotations during launch [4]. For the DM13 projectile, we are exploring a few millisecond-long, asymmetric pressure loads on the dynamic response of the projectile. Except for the five-petalled fin arrangement, the projectile is axisymmetric. These factors contribute to choosing a two-dimensional linear elastic beam model for the rod portion of the DM13 (fins, penetrator, windscreen and tip), subject to

a transverse short-duration blast load supported by a discretized Winkler foundation, which idealizes the sabot's spring like behavior. Although we lose robustness by not materially or geometrically modeling the sabot, we simplify the modeling conceptually and, more importantly, capture the behavior of the rod as it interacts with the sabot.

Modeling the geometry and material properties of the fins, rod, windscreen, and tip is a straightforward process. Using a disassembled projectile (as shown in Fig. 2), we measure dimensions to obtain geometric properties. We use reference values for Young's modulus 7075 aluminum, 1010 steel and tungsten, and modify values for densities based on actual weight and volume measurements of the fins separately and the rod, windscreen and tip together. The Young's modulus and density values are listed to Table 2.

To estimate the effective stiffness of the sabot on the rod, we develop a linear spring model of the sabot–rod interaction and perform a simple experiment on the DM13 to estimate the spring constant. We assume that the sabot acts as a series of linear springs over the 15.24 cm contact length between the rod and the sabot. Because there are 35 threads in this region and hence 35 contact points, we assume 35 linear springs to be uniformly spaced at 0.40 cm. Each spring deflects a small amount under an applied load. When an eccentric load is applied to the rod (near the fins or the tip for example), the rod bends and rotates as a rigid body. For small loads, bending of the rod is negligible. The rod's rigid body rotation still causes each spring to deflect; these deflections are proportional to the rod's rotation. Figure 9 shows a diagram of the rod undergoing a rigid body rotation, θ, thereby compressing and extending the supporting springs. By determining the rotation in the rod under a known loading, we can infer an effective stiffness for each spring, and hence for the entire sabot. To do this, we conducted a simple experiment.

The experimental set-up, conducted at Harry Diamond Laboratory, is depicted schematically in Fig. 10; a photograph is shown in Fig. 11. We clamped a DM13 projectile to a table and positioned two dial gages 6.40 cm apart to measure the vertical displacement of the tip; these displacements were induced by hanging weights, as shown in Fig. 10. To determine the rotation angle, we divided the difference between the dial gage readings by the spacing distance between them. The data are plotted in part in Fig. 12. The equivalent rotational stiffness curve-fits to be 201 000 N/rad. For the smaller loads (<200 N), this is equivalent to a stiffness of about 438 ± 87.6 kN/mm for each of the 35 springs. The sizeable variation (20%) in k is due to the variation in the number of springs acting in tension and

Table 2. Material properties of DM13 projectile

Component	*Material*	*Density (g/cc)*	*Young's modulus (MPa)*
Fin, tip, sabot	7075-T6 Aluminum	2.88	68.9
Rod	Tungsten	18.0	351.4 E3
Windscreen	1010 Steel	7.85	206.8 E3

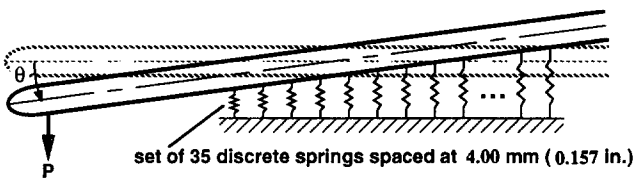

Fig. 9. Schematic of idealized rod undergoing a rigid body rotation θ, due to load P, being supported by 35 springs each with spring constant k. The undeflected and unloaded rod is shown in the dotted outline.

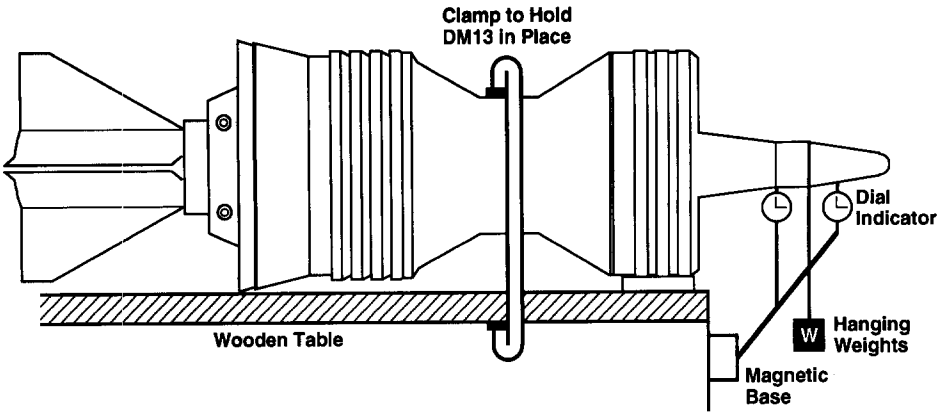

Fig. 10. Schematic of static test setup for inferring equivalent stiffness of sabot. Dial indicators separated by 6.4 cm.

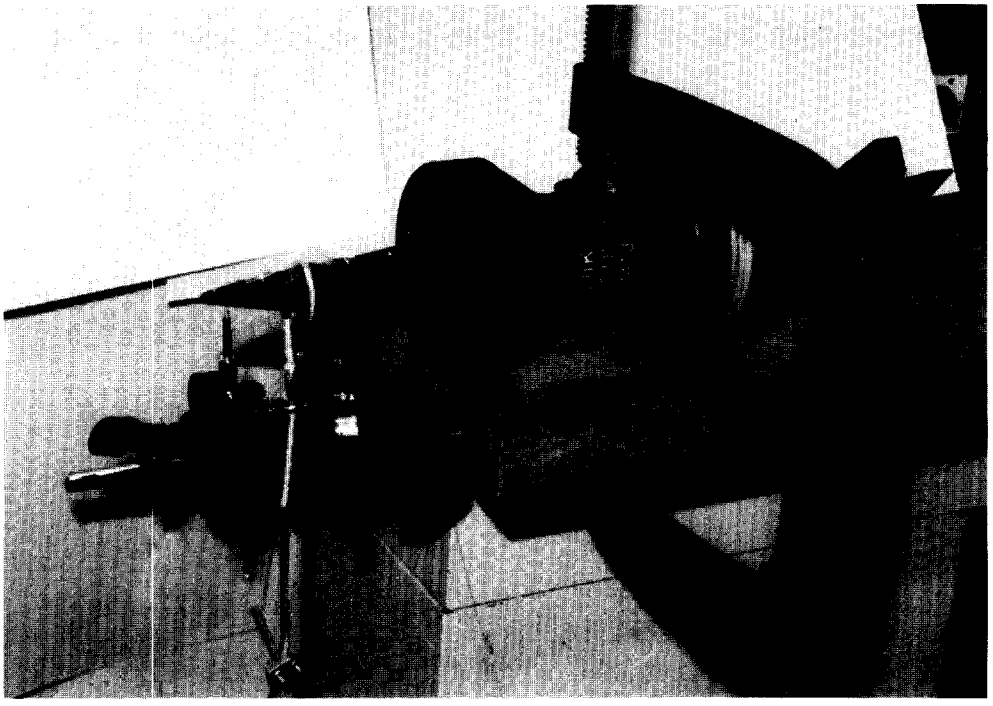

Fig. 11. Photograph of static test set-up.

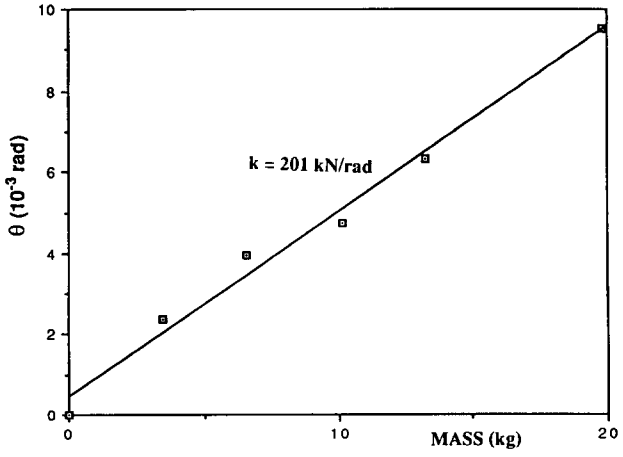

Fig. 12. Plot of test data showing linear relation between applied load and rod rotation.

compression for each load and the limited precision of the experiment. For larger loads, bending in the rod is not negligible and the stiffness results become less accurate. We model the rod alone in our finite element analysis and treat the sabot as a series of springs.

To simulate the asymmetric pressure loading on the beam model, we assume a conservative 2% asymmetry of the blast pressure magnitude and project the pressure distribution over the surface area of the fin [3]. The duration of this asymmetry is 4 ms. Because these data come from experiments where pressure readings are noisy and not repeatable [13], this 2% asymmetry and the 4 ms time duration are conservative to ensure the worst-case loading. The equivalent distributed load is shown in Fig. 13, where the peak magnitude, which occurs at 4 ms, is 700 000 N/m. We assume the distributed load to act uniformly over the aft 7.6 cm portion of the tail but increase by a constant 14% over the next 3.8 cm. The reason for this step increase in magnitude is the step increase in surface are of the projectile just after of the rear obturator (which seals off the pressure and terminates the asymmetric loading on the projectile).

Figure 14 shows the tapered beam model with the loading applied and the support springs attached. The ANSYS finite element model contains 506 nodes, 470 tapered beam elements (each 1 mm long) and 35 spring elements. For the linear transient analysis, we

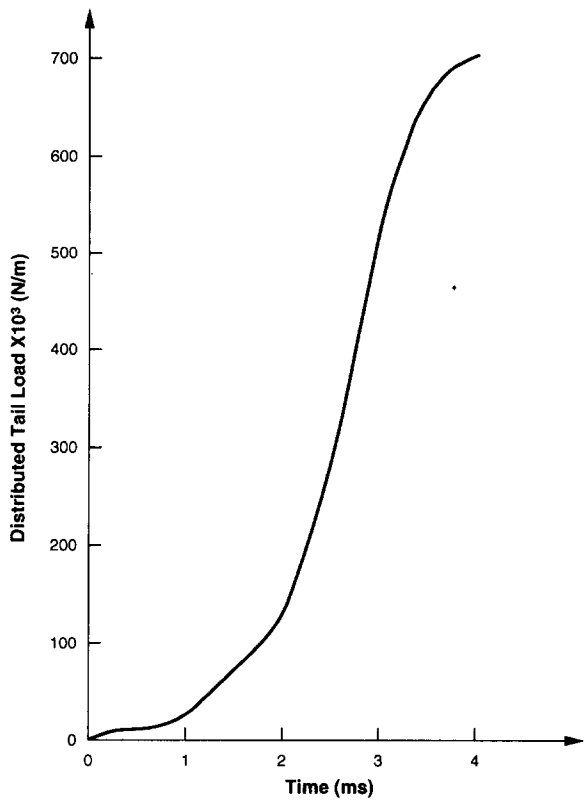

Fig. 13. Plot of equivalent loading on tail portion of model.

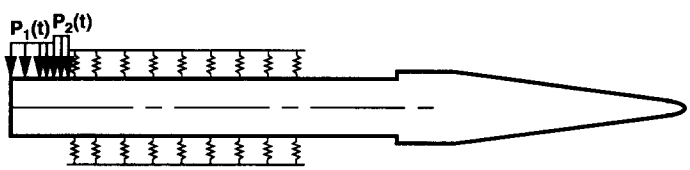

Fig. 14. Schematic of ANSYS model, shown with equivalent asymmetric loading and equivalent sabot stiffness.

employ a time step of 10 ms. This value is about 1% of the fourth measured period of the projectile, which Berman determined experimentally using modal analysis [14]. We ignore damping because of the short (8 ms) duration of the time history.

Figures 15 and 17 show two displacement–time histories, and Figs 16 and 28 show two velocity–time histories for locations corresponding to the tip, tail, and the first sabot contact point (SP01). Displacements and velocities are measured relative to the projectile coordinate system. In Figs 16 and 17, the time histories shown correspond to the lower bound for the sabot stiffness, which is 4.38×10^6 N/m. We assume the muzzle exit occurs at 7.2 ms.

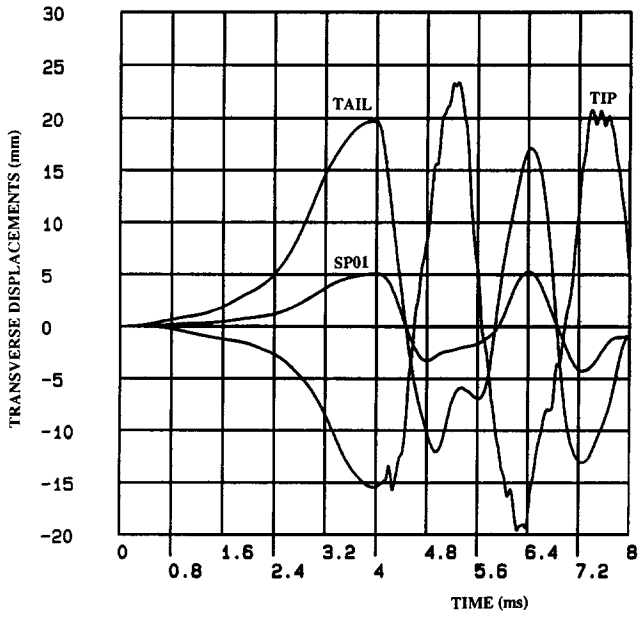

Fig. 15. Displacement time histories for tip, tail, and SP01, assuming sabot stiffness of 4.38×10^6 N/m. Time step is 1×10^{-5} s. Positive displacement is down. Displacements are measured from the center line of the projectile.

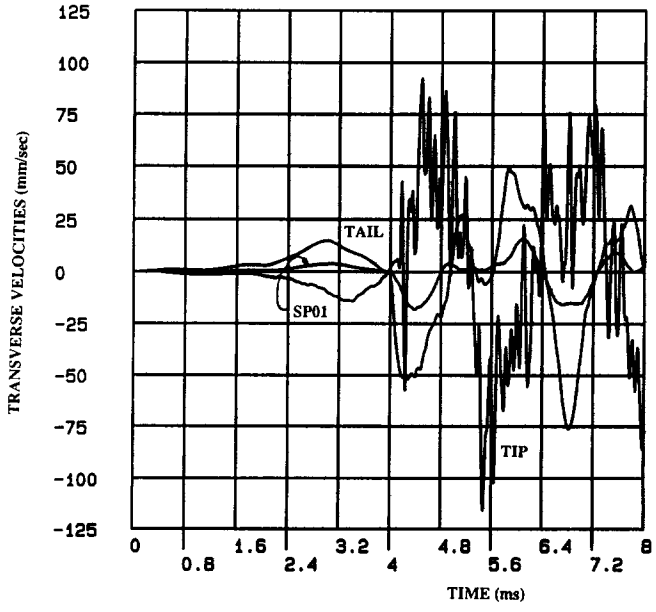

Fig. 16. Displacement time histories for tip, tail, and SP01, assuming sabot stiffness of 4.38×10^{-7} N/m. Time step is 1×10^{-5} s. Positive displacement is down. Displacements are measured from the center line of the projectile.

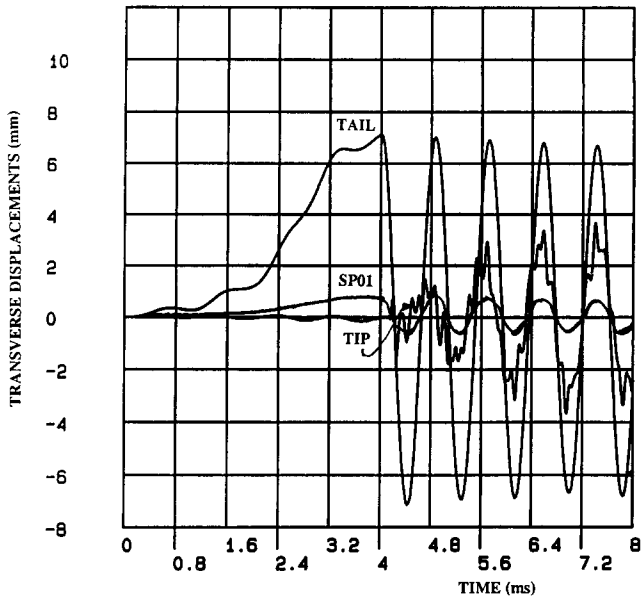

Fig. 17. Velocity time histories for tip, tail, and SP01, assuming sabot stiffness of 4.38×10^6 N/m. Time step is 1×10^{-5} s.

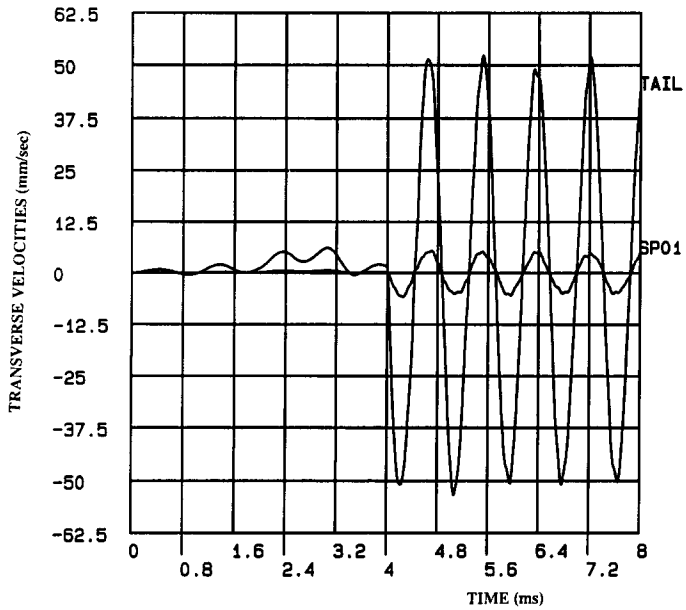

Fig. 18. Velocity time history for tail and SP01, assuming sabot stiffness of 4.38×10^7 N/m. Time step is 1×10^{-5} s.

As expected, all three points undergo smooth displacement rises similar in shape to the loading curve before going into free vibration [15]. The peak displacement for the tail is 20 mm; this occurs at the peak load termination point of 4 ms. The 5 mm peak displacement of SP01 appears large, but the DM13 has enough "play" in the rod-sabot system that a 5 mm displacement of the rod is certainly possible. During the free vibration phase, all three points oscillate with some energy transfer between tip and tail. At muzzle exit, both the tip and tail have displacements of about 13 mm which represents about 70% of the peak displacement. The period of oscillation is about 2.4 ms, which falls within 10% of the observed natural petiod in the first mode [14].

The change in material properties and the tapered tip cause the noise in the tip displacement history in Fig. 15; in Fig. 17, this phenomenon manifests itself in the tip velocity history. Although the tail's velocity at launch is close to zero, the tip velocity is close to 75 mm/s.

For comparison, Fig. 16 shows displacement–time histories of the tip, tail, and SP01, with the effective sabot stiffness undergoing a ten-fold increase in magnitude to 4.38×10^7 N/m. As expected, the overall response magnitudes of the system are less than for the more flexible system; for example, the peak amplitude of the tail is about 7 mm. The peak tip displacement amplitude is initially 1/7 that value and increases during the 8 ms time history to about half the peak response of the tail. This transfer of energy occurs because of the stiffer springs in this model. The stiffer system also manifests itself in the period of vibration, which is now at about 0.8 ms. Curiously, all three points vibrate in phase. In fact, for this particular set of time histories, the tip, the tail, and SP01 have zero displacement at muzzle exit. The peak velocity occurs at this point; its value for the tip is about 35 mm/s; Fig. 18 shows the overall velocity time histories for the tail and SP01.

4. SUMMARY AND CONCLUSIONS

We describe two dynamic in-bore response analyses of the DM13 projectile, a low-cost kinetic energy projectile with good accuracy performance. In the first analysis, we assume that the projectile is forced to translate three nonstraight launch tubes as a rigid body undergoing small rotations. Having developed the theory and simulation describing such motion, we present results where angular rotations relative to the gun tube orientation reach 8×10^{-4} rad and angular velocities can be as high as 3 rad/s. The magnitudes of these values compare well with values generated from detailed three-dimensional finite element analyses [3].

In the second analysis, we explore the in-bore transient transverse vibrations of a finite element model of the rod due to pressure loading asymmetry. We find that a 2% base pressure asymmetry produces considerable transverse displacements in the rod tail and tip. Peak displacements vary with the effective stiffness of the sabot. Peak transverse velocities approach 100 mm/s an peak displacements exceed 20 mm. These values represent transient vibrations that damping will cause to decay in time; however its effects on projectile performance need to be determined.

The two principal conclusions we draw from these efforts are as follows:

Launch tube nonstraightness induces rigid body rotations of the projectile during in-bore travel. The magnititudes of these rotations may or may not increase with the severity of the launch tube profile.

Base pressure asymmetry induces vibrations in the DM13 projectile. Strongly affecting these vibrations is the sabot stiffness. Energy is transferred from the tail to the tip during the launch, creating larger amplitudes in the tip displacement at muzzle exit.

Acknowledgements—The research reported herein was made possible by the US Army Summer Faculty Fellowship Program, Contract No. DAAl 03-91-C-0034, Task Control No. 93303. I am grateful for the support and resources provided by Drs Bruce Burns and Stephen Wilkerson at Aberdeen Proving Ground, Maryland and thank Nina Duan and Mark Deshon, both from the University of Delaware for their help with the graphics.

REFERENCES

1. D. A. Rabern, Axially accelerated sabot rods subjected to lateral forces. BRL-CR-671, U.S. Army Laboratory Command, Ballistic Research Laboratory, Aberdeen Proving Ground, MD (1991).
2. S. E. Powell, The theoretical modelling of the dynamics of initially non-straight barrels using finite difference techniques. *Proc. Fifth US Army Symp. on Gun Dynamics*, San Diego, CA (1987).
3. D. A. Rabern and J. R. Neal, Numerical simulations of gun-launched kinetic energy projectiles subjected to asymmetric base pressure. BRL-CR-677, U.S. Army Ballistic Research Laboratory, Aberdeen Proving Ground, MD (1991).

4. D. A. Rabern, Numerical simulations of gun-launched kinetic energy projectiles subjected to asymmetric base pressure. *Int. J. Impact Engng* **12**, 3 (1992).
5. Sabot Technology Engineering, *Engineering Design Handbook*, AMP Pamphlet 706-445, Department of the Army, Washington, DC (1972).
6. R. P. Kaste and S. A. Wilkerson, An improved sabot design and DYNA3D analysis for the XM900E1 kinetic energy projectile. BRL-TR-3359, U.S. Army Ballistic Research Laboratory, Aberdeen Proving Ground, MD (1992).
7. D. A. Rabern, Axial and lateral impulsive loading of kinetic energy projectiles during launch—Part II. Numerical simulations. *Int. J. Impact Engng* **12**, 1 (1992).
8. G. W. Housner, The behavior of inverted pendulum structures during earthquakes. *Bulletin of the Seismological Society of America* **53**, 2 (1963).
9. M. Aslam, W. Godden and D. T. Scalise, Earthquake rocking response of rigid bodies. *J. Structural Division*, ASCE **106**, ST2 (1980).
10. R. H. Allen, I. J. Oppenheim, A. R. Parker and J. Bielek, On the dynamic response of rigid body assemblies. *Earthquake Engineering and Structural Dynamics*, Vol. 14, No. 6, pp. 861–876 (1986).
11. K. Ogata, *System Dynamics*. Prentice Hall, Engelwood Cliffs, NJ (1992).
12. S. A. Wilkerson, Private communication (1993).
13. R. P. Kaste, Private communication (1993).
14. M. Berman, Private communication (1993).
15. R. Clough and J. Penzien, *Structural Dynamics*, McGraw Hill, New York (1975).